Interplay between boron doping and epitaxial relationships in VO 2 films grown by laser ablation

Aude Bailly, Pierre Bouvier, Stéphane Grenier, Thameur Hajlaoui, Michael Gaudin, Aline Y. Ramos, Mohamed Chaker, Laetitia Laversenne

Interplay between boron doping and epitaxial relationships in VO_2 films grown by laser ablation

A. Bailly [a], P. Bouvier [a], S. Grenier [a], T. Hajlaoui [b], M. Gaudin [a], A. Y. Ramos [a], M. Chaker [b], L. Laversenne [a]

[a] *Univ. Grenoble Alpes, CNRS, Grenoble INP, Institut Néel, 38000 Grenoble, France*
[b] *Institut National de la Recherche Scientifique, Centre Energie Matériaux & Télécommunications, Université du Québec, Varennes, Québec PQ J3X 1S2, Canada*

Abstract

In this contribution, the effect of boron doping on the functional and structural properties of VO_2 thin films is investigated. Temperature-dependent measurements were performed on pure and boron-doped (0.5 and 1.3 at.%) VO_2 films grown on Al_2O_3(0001) by Reactive Pulsed Laser Deposition. Increasing the boron concentration leads to a noticeable decrease of the transition temperature (by $\sim$ 12°C), accompanied by a significant modification of the hysteresis loop shapes. The phase transition occurs at *ca.* 73 °C in the undoped film, while it drops down to *ca.* 60 °C in the film containing the highest boron amount. The undoped sample exhibits the best resistivity contrast (about 4 orders of magnitude) with a relatively narrow hysteresis cycle ($\sim$ 6 °C). The most doped sample has a broad and significantly reduced resistivity contrast (less than 3 orders of magnitude). Raman spectroscopy and high-resolution X-ray diffraction were performed to elucidate the nature of the involved phases and their structure. A correlation was found between increasing the boron concentration and the formation of two peculiar in-plane epitaxial relationships; the VO_2 films evolving from one to the other. We also evidenced the presence of the transient M2 phase in the most doped sample.

Keywords:
Boron-doped VO_2 films, Epitaxial growth, Metal-to-insulator transition, Temperature-dependent measurements, X-ray diffraction, Raman spectroscopy.

1. Introduction

Vanadium dioxide in its bulk form exhibits a reversible insulator-metal transition (IMT) at a critical temperature T_{IMT} of 68°C. The drastic change of the electrical resistivity goes along with a crystallographic phase transformation, changing from the insulating monoclinic M1 phase below T_{IMT} to the metallic tetragonal R (rutile) phase beyond. The optical transmittance in the infrared range is also strongly affected, as VO_2 reversibly switches from transparent below T_{IMT} to opaque above it. Based on

these peculiar optical and electrical thermally-driven changes, many applications are targeted, such as : thermochromic windows Zhou et al. [1], optical fibers [2] or passive radiators [3]. For these developments, VO_2 films are usually deposited on amorphous or crystalline substrates. In this latter case, the possible existence of specific epitaxial relationships between the VO_2 film and the substrate provides invaluable opportunities to tailor the film properties *via* strain engineering [4].

Chemical doping of VO_2 is another strategy to tune its electrical and optical properties. The objectives of elemental doping are twofold: i) electronic, by increasing a carrier concentration and ii) structural, by inducing atomic cell distortions. The nature of the dopant element (size and valence) plays a crucial role [5]. Numerous studies report on the influence of substitutional doping with high-valence metallic cations, such as W, Re or Mo. Experimental studies related to doping with light elements are instead very scarce. Actually, introducing such light elements into the VO_2 structure is experimentally challenging since they are either too light (as B) or too volatile (as N and C), which explains why most studies deal with heavier elements. Hydrogenation induces the formation of the metallic R phase at temperatures much lower compared to pure VO_2, even at room temperature depending on the hydrogen concentration [6, 7, 8]. For boron-doped VO_2, the insulator-metal transition was theoretically investigated by Density Functional Theory (DFT) calculations [9, 10]. It was demonstrated that the boron atoms sit in interstitial positions within the VO_2 lattice and that a strong decrease of the transition temperature should be expected. B-doped VO_2 samples were obtained in different forms following various synthesis techniques: boron incorporated by diffusive doping into nanobeams and nanoparticles [11], thin films doped by ion implantation [12], nanoparticles obtained by hydrothermal synthesis [13]. Some coworkers in the present study recently reported on the evolution of the insulator-metal transition of VO_2 films doped with low amounts of boron (up to 1.6 at. %) [14]. The B-doped VO_2 films were synthesized by Reactive Pulsed Laser Deposition (RPLD) on Si(100) substrates. The IMT temperature is drastically reduced due to the boron doping ($\sim$ 31 °C / at. %), characterized by interstitial atoms in the VO_2 lattice. The transition temperature T_{IMT} even drops down to 17.5 °C for 1.6 at. % of boron. The 4^+ valence of the vanadium atoms is kept, whatever the boron concentration; but the incorporation of boron into the VO_2 lattice tends to stabilize the R phase at much lower temperature compared to bulk VO_2. In the present paper, the effect of the two factors (B doping and epitaxial growth) on the functional and structural properties of RPLD-synthesized VO_2 films on Al_2O_3(0001) is investigated. The temperature-dependent measurements highlight the evolution of the phases nature and their epitaxial relationships, as a function of the boron concentration and temperature.

2. Experimental details

Sample synthesis

Pure and boron-doped VO_2 films have been synthesized using PLD on c-oriented sapphire substrates ($Al_2O_3(0001)$) by ablating vanadium and mosaic vanadium/boron targets [14]. A KrF excimer laser beam (wavelength of 248 nm and pulse duration of 25 ns) was focused on the targets at a repetition rate of 10 Hz. Sapphire substrates were used due to their lattice parameter that allows the epitaxial growth of VO_2 films (mismatch $\sim$ +4 %) as well as for their high resistivity, making them appropriate for resistivity measurements of the deposited films. During deposition, the targets were placed at a distance of 6.5 cm in front of the substrate, while the laser beam was focused on the target forming a 1.65 mm^2 spot size that results in a laser fluence of 2 $J.cm^{-2}$ on target. To improve the uniformity of both target ablation and films thicknesses, the laser beam was scanned across the target and both substrate and targets were maintained in a rotating motion during deposition. To achieve well-crystallized and epitaxial films, the substrate temperature and the background oxygen pressure were kept at 500 °C and 30 mTorr, respectively. The final film thickness was in the range 80-100 nm. The boron concentration was determined by X-ray Photoelectron Spectroscopy (XPS), with an accuracy of $\pm$ 0.1 at. %, and boron atoms have been shown to sit in interstitial positions [14]. Three samples are studied hereafter: pure VO_2 and VO_2 doped with 0.5 at. % and 1.3 at. % of boron. They are respectively called B0, B05 and B13.

X-ray diffraction

The X-ray diffraction (XRD) experiments were performed with two distinct set-ups. The room-temperature (RT) specular scans were recorded with a *D8 Advance* X-ray diffractometer (Bruker), with Cu $K_{\alpha 1}$ radiation (λ= 1.54056 Å), in a Bragg-Brentano $\theta/2\theta$ geometry, equipped with a Johansson monochromator and a linear *Lynxeye* detector. Reciprocal space mapping and temperature-dependent XRD measurements were performed with a high-resolution X-ray diffractometer (SmartLab, Rigaku Corp.) equipped with a 9 kW rotating Cu anode and a 5-circle goniometer, in a parallel beam mode. The oven used for temperature cycles (Anton Paar; accuracy $\pm$1°C) was capped with a carbon dome, flushed and then swept by a slight nitrogen flux to avoid sample oxidation. Extrinsic thermal effects were counteracted by systematically checking the sample surface alignment with respect to the incident X-ray beam and optimizing the measured reflections at each temperature. The experimental set-up and the scan types performed are thoroughly described in a previous paper [15]. Crystalline phase identification was also done by recording specular $\theta/2\theta$ scans. In this case, a 2-bounce Ge(220) crystal was used for monochromatization on the Cu $K_{\alpha 1}$ emission line. Finally, a specific configuration allows to record the diffraction signal arising from lattice planes perpendicular to the sample surface. The in-plane epitaxial relationships

of the VO_2 films with respect to the $Al_2O_3(0001)$ substrate can thus be determined. In this case, the Ge monochromator was removed to increase the count rate and the grazing incidence angle was fixed to $\sim 0.3°$.

Raman spectroscopy

Unpolarized Raman scattering experiments have been performed in a backscattering geometry with the final stage of a Horiba T64000 spectrometer using a 1800 grooves.mm^{-1} grating (blazed at 500 nm) and rejecting the Rayleigh line with an edge dichroic beamsplitter (LP02-514RE-25 RazorEdge, Semrock). This allowed to measure a relative wavenumber range of 100 to 750 cm^{-1}. The entrance slit was 100 µm-wide providing a spectral resolution of 0.7 cm^{-1}. The spectrometer was calibrated in wavenumber by using the 520.6 cm^{-1} phonon of a Si(100) reference wafer. A continuous argon laser beam (Spectra Physics, λ = 514.5 nm) was focused onto the VO_2 film into a spot of 2 to 4 µm in diameter, using a long-distance lens (Olympus $\times$50 magnification). The laser power was adjusted to 0.25 mW in front of the lens to ensure a good signal and to avoid any thermal effect that could trigger the insulator-metal transition. The sample temperature was cycled by using a temperature-controlled stage (Linkam, THMS 600 controller) in the range 25°C - 85°C. The sample chamber was swept with argon to avoid a phase transformation towards V_2O_5 or V_6O_{13}, often observed when VO_2 is heated in air [16]. The spectral parameters (wavenumber, half-width at half maximum and area) were obtained from the decomposition of each spectrum with several Lorentzian peaks and a linear background using the Fityk software [17]. The accuracy on the wavenumber values was estimated to be $\pm$ 0.2 cm^{-1}.

Fourier transform infrared spectroscopy

The Fourier transform infrared (FT-IR) spectroscopic measurements were performed at the CARMALIM platform (IRCER Laboratory, University of Limoges). A Thermo Fischer Scientific spectrometer (Nicolet 6700), equipped with a specular reflection accessory (Harrick Scientific ERA 12°), was used. The temperature was cycled using a Peltier sample stage with a LFI-3751 temperature controller and the reflectivity was collected at a wavelength of 3 μm. The background level was calibrated on a c-oriented bare sapphire substrate.

3. Results and discussion

3.1. Morphological and electrical properties

The four-point probe resistivity measurements, as well as Scanning Electron Microscopy (SEM) images of the VO_2 films, are shown in Fig. 1. Boron doping clearly affects the grain morphology: the higher the boron concentration, the smaller the grains.

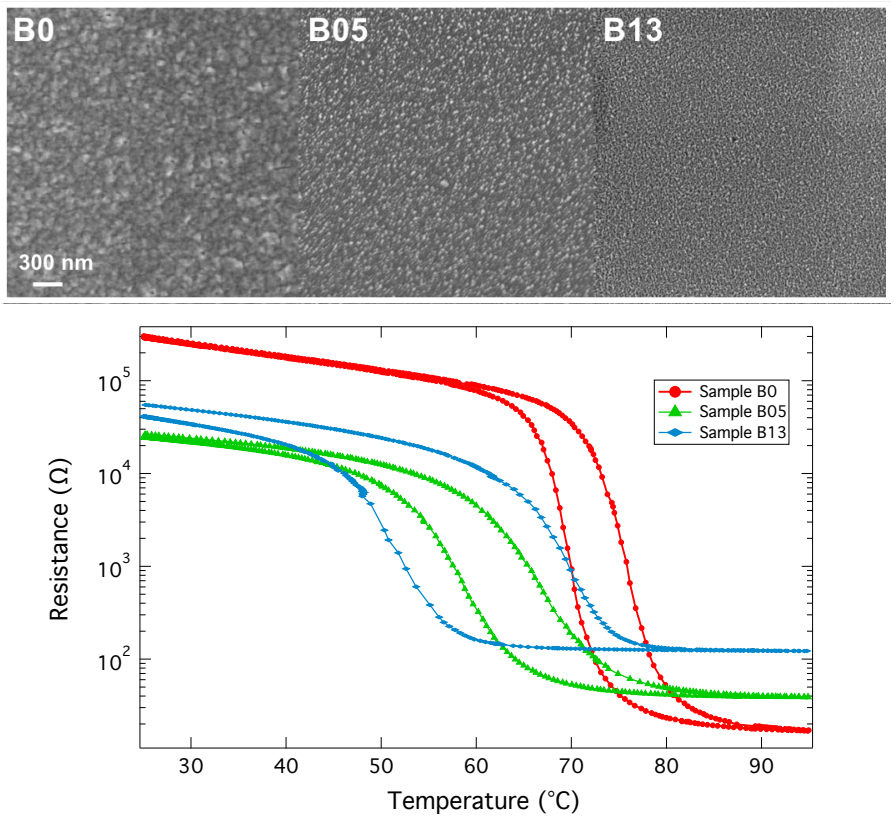

Figure 1: (Top) SEM images of the pure and boron-doped VO_2 samples. From left to right: undoped VO_2 (*B0*), doped with 0.5 at. % of B (*B05*) and 1.3 at. % of B (*B13*). (Bottom) Electrical resistance as a function of temperature.

We observe that the incorporation of boron effectively decreases the transition temperature averaged between heating and cooling cycles. T_{IMT} drops from 72.6 °C (+/- 0.1 °C) for the undoped sample to 62.3 °C and 60.5 °C for the 0.5 at.% and 1.3 at.% boron-doped samples, respectively. However, increasing the boron concentration in the films induces a significant decrease of the resistivity contrast (from more than 4 orders of magnitude to less than 3), as well as a broadening of the hysteresis width (6 °C, 8 °C and 18 °C for the B0, B05 and B13 samples, respectively). Overall, there is no simple trend of the electric properties with respect to the B doping in these films.

The evolution of the transition temperature with the amount of boron inserted in the VO_2 lattice might seem surprising as T_{IMT} does not decrease linearly with the increase of the boron concentration. We also note that the transition temperatures of our samples are substantially higher than the ones already reported in the literature [11, 13, 14], except Ufert *et al.* who do not observe any effect of boron doping on the transition temperature [12]. Several parameters are known to influence T_{IMT}, such as the synthesis technique and conditions (impacting among other things the vanadium valence state and the amount of intrinsic point defects), the existence of strains in the material (induced by epitaxy or doping) and the eventual addition of a dopant element. In the case of boron doping, it was recently suggested that thermal and time histories might play a crucial role as interstitial boron atoms could diffuse in the VO_2 lattice, leading to a gradual modification of both T_{IMT} and resistivity [18] (and references therein).

3.2. Identification of the VO_2 phases through the IMT

Temperature-dependent Raman spectroscopy was used to identify the VO_2 phases appearing during the insulator-metal transition. The Raman spectra of the B13 sample recorded upon heating from 25°C to 80°C are reported in Fig. 2. When increasing the temperature, we observe a progressive disappearance of the monoclinic phase Raman signature toward an almost featureless spectrum, revealing the transition to the high temperature metallic rutile phase. The Raman spectra recorded for the B0 and B05 samples behave qualitatively the same and are therefore not shown.

The VO_2 monoclinic M1 (point group: C_{2h}^5) and the rutile R (point group: D_{4h}^{14}) phases exhibit very different Raman signals. The M1 phase is characterized by 18 Raman active modes (9 A_g and 9 B_g) [19, 20, 21, 22, 23]; some of which being very intense such as $A_g(1)$ at 194 cm^{-1}, $A_g(2)$ at 225 cm^{-1}, $A_g(3)$ at 310 cm^{-1} and $A_g(6)$ at 620 cm^{-1}. The R phase exhibits broad Raman modes (at 140 cm^{-1}, 450 cm^{-1}, 655 cm^{-1} and 850 cm^{-1} for B_{1g}, E_g, A_{1g} and B_{2g}, respectively) [24, 25] that are hardly measurable because of its metallic nature. The monoclinic M2 phase (point group: C_{2h}^3) was first examined by Raman spectroscopy in chromium-doped VO_2 [26]. This phase is expected to display as many Raman modes as the M1 phase, but with an upshift of $A_g(1)$ (to 201 cm^{-1}) and $A_g(2)$ (to 228 cm^{-1}), as well as a downshift of $A_g(3)$ (to 296 cm^{-1}) [27, 28, 29]. Similar wavenumber shifts were interpreted as an effect of the oxygen stoichiometry [30]. The establishment of the M2 phase presence is often based only on

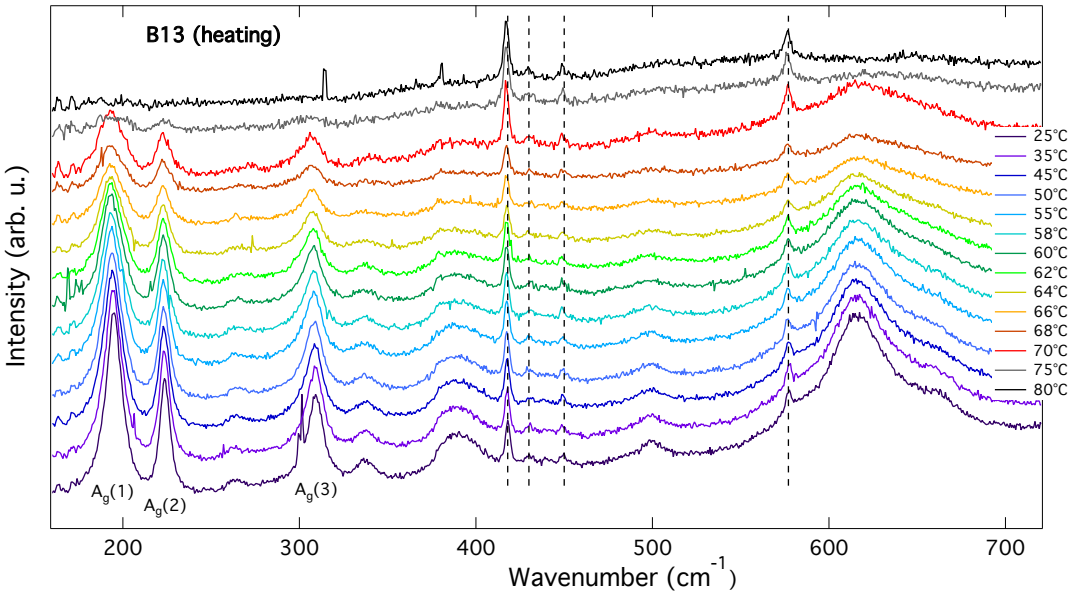

Figure 2: Raman spectra of the B13 sample recorded upon a heating step. The three VO_2 A_g modes of interest for our purpose have been indicated and the main Raman modes of the $Al_2O_3(0001)$ substrate are indicated by dashed lines.

the observation of the 640 cm^{-1} Raman peak [31]. However, this mode is much broader than the low wavenumber modes and it is located in a wavenumber region where at least three peaks of the M1 phase are also present. For these reasons, we consider that this unique criterion is not strong enough to draw an unambiguous conclusion. We believe that the temperature evolution of the low wavenumber Raman modes of VO_2 (which involve mainly vanadium displacements) is more accurate for studying the appearance of the transient M2 phase, even though this frequency range is in practice more difficult to access (spectrometer cut-off generally around 200 cm^{-1}).

The temperature dependence of the integrated total area of the monoclinic Raman modes ($A_g(1)$ + $A_g(2)$) is shown in Fig. 3 along with the electrical resistance measured simultaneously between two tungsten probes inside the Linkam heating stage. The observed hysteresis loops are typical of the first-order insulator-to-metal transition. In the case of B13, it is interesting to note that the Raman intensity of the ($A_g(1)$ + $A_g(2)$) modes does not exactly follow the electrical resistance measured concomitantly during the heating step, unlike the undoped or weakly doped samples (B0 and B05). The "excess" in the Raman intensity progressively vanishes while approaching the IMT.

The reflectivity in the mid-infrared region at 3 μm is shown in Fig. 3 (bottom right), while cycling the samples between RT and 90 °C. The transition from the insulating to the metallic state is illustrated via the change of the reflecting properties with tempera-

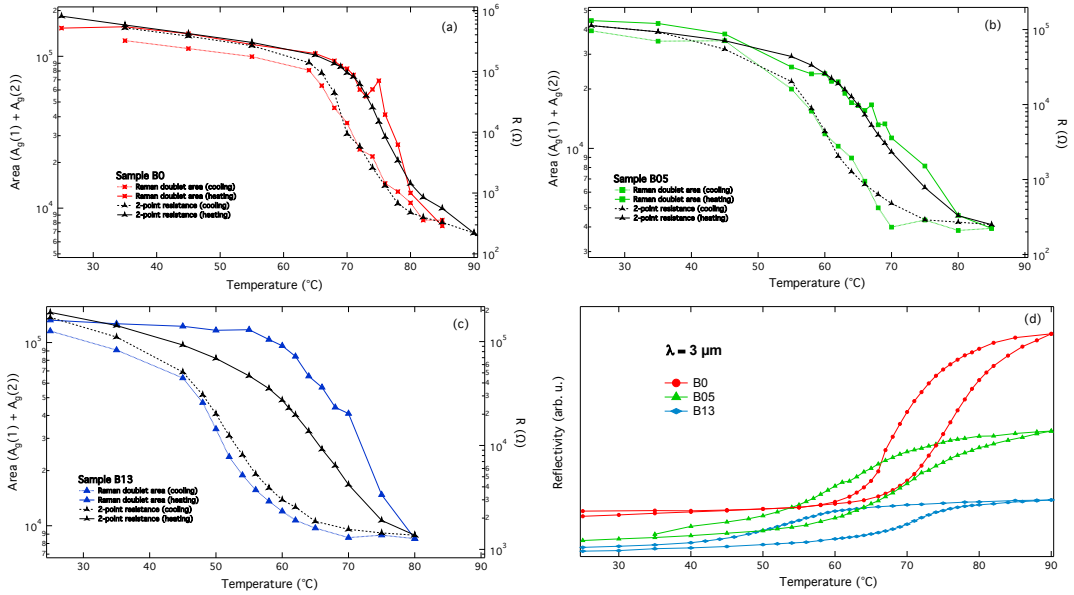

Figure 3: (a) to (c) Raman doublet area (left vertical scale) and electrical resistance (right vertical scale) as a function of temperature for different doping concentrations; (d) Reflected intensity at 3 μm as a function of temperature.

ture. Close to room temperature, the incident beam is poorly reflected by the surface of the VO_2 films which appear to be almost transparent at this specific wavelength and the pure VO_2 sample exhibits a sligthly higher reflectivity. When increasing the temperature, the films gradually get metallic, leading to an increase of the reflectivity. Whatever the temperature, the B13 sample is much less reflective than the two other samples. Qualitatively, the width and amplitude of the hysteresis observed for each sample are similar to the general trend described by the electrical measurements.

Fig. 4 shows the temperature dependence of the $A_g(1, 2, 3)$ phonon wavenumbers of the monoclinic M1 phase measured in the B0, B05 and B13 samples, as well as for a reference bulk VO_2 single-crystal. The crystal displays the classical wavenumber temperature downshift which is the typical behavior expected from anharmonic effect [32]. In the temperature range explored during our measurements (25 to 85°C), the wavenumber temperature dependence can be described by a linear function as indicated by the full black line in Fig. 4. It is worth noticing that the Raman modes of the $Al_2O_3(0001)$ substrate measured at 441 and 586 cm^{-1} through the VO_2 films show the same linear downshift when the temperature increases (not shown).

Up to roughly 10-15°C before the transition to the rutile phase, the three $A_g(1, 2, 3)$ Raman modes measured in the films display the same linear downshift of their wavenumber. However, when approaching the IMT, the B13 sample differs from the less doped ones (B0 and B05). We observe that the $A_g(1)$ and $A_g(2)$ Raman modes shift

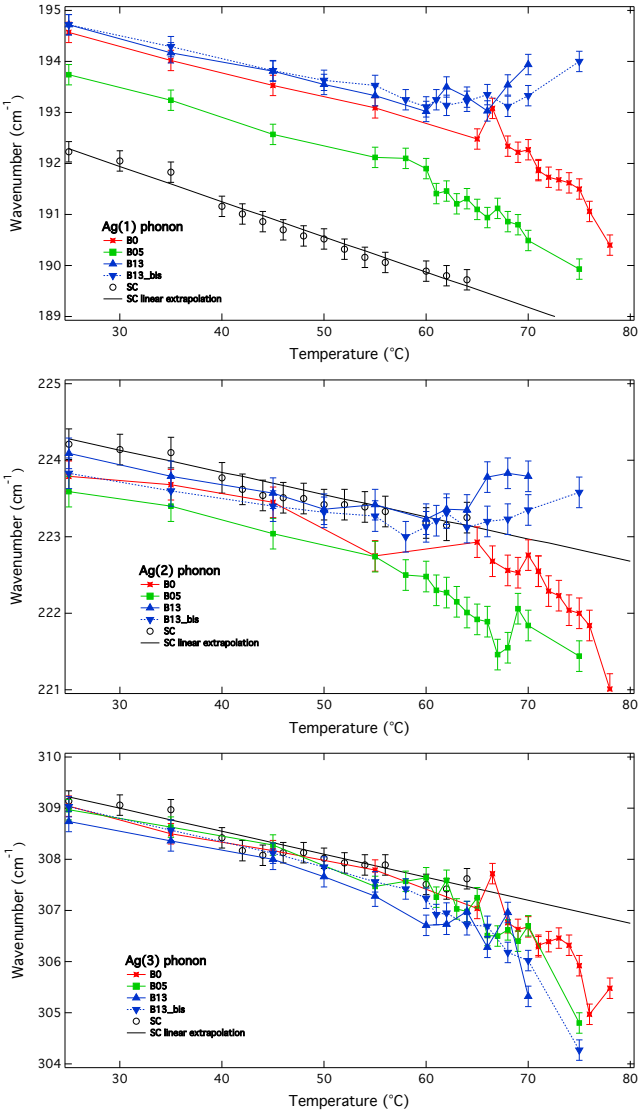

Figure 4: From top to bottom : Evolution of the wavenumbers of the $A_g(1)$, $A_g(2)$ and $A_g(3)$ phonons as a function of temperature, for the three films and a bulk VO_2 single-crystal (SC). Full and dashed lines are guides for the eyes. The M2 phase is evidenced in the case of the B13 sample at ~ 65°C, through an upshift of the $A_g(1)$ and $A_g(2)$ phonon wavenumbers.

in the opposite direction compared to what is expected considering only the temperature effect. The fact that these two modes shift upwards, whereas the $A_g(3)$ mode shifts downwards, suggests that the monoclinic M2 phase is present before the transition to the rutile phase. The appearance of the M2 phase also supports the observation made earlier in Fig. 3, regarding the gap observed between the Raman intensity and the electrical resistance. The Raman intensity of the ($A_g(1)$ + $A_g(2)$) modes does not allow to differentiate the M1 and M2 phases because both exhibit intense Raman signatures in this energy range. Only the dependence of these two modes on temperature allows to confirm the presence of the M2 phase. This was already proposed in a previous work dealing with an undoped VO_2 film and involving some of the co-authors of the present article [15]. This is also well explained by Okimura *et al.* who observed that the 195 cm^{-1}, 224 cm^{-1} and 620 cm^{-1} phonon modes of the M1 phase display a phonon hardening above a given temperature, whereas the corresponding phonon modes of the M2 phase exhibit a standard behavior due to the lattice thermal expansion (see Figure 4 in Ref. [33]). The convergence of the M1 phase Raman wavenumbers towards the ones of the M2 phase indicates that the low temperature M1 phase transforms to the rutile one via a transient structure similar to the M2 phase. The same upshifts of the 195 cm^{-1}, 225 cm^{-1} and 620 cm^{-1} phonons were described as a fingerprint of the T-M2 transformation in [100]-oriented single crystalline nanobeams on r-cut sapphire substrates with temperature [34]. These upshifts were also interpreted as a transformation to a triclinic cell as a bridge between M1 and M2 monoclinic phases in individual, homogeneous VO_2 single crystalline microbeams grown on a silicon substrate [35]. The authors proposed that, regardless the VO_2 film strain state, the monoclinic M2 structure is an ubiquitous phase for the transition to the rutile phase. The M2 phase formed prior to the IMT was also proposed based on the same wavenumber shifts for VO_2 films of different thicknesses deposited on c-cut sapphire substrates [36]. Using the phenomenological Landau model, Tselev *et al.* [37] explained that the M1 and M2 phases are two different ways to respond to the same instability of the rutile lattice. Consequently, while M1 is the stable lower-symmetry phase of unstrained VO_2 in ambient conditions, a small perturbation can stabilize the M2 phase with respect to the M1 phase or bring the M1, M2 and R phases to coexist. In our case, it is interesting to notice that the $A_g(1)$ Raman modes (at 193-195 cm^{-1}) observed for the three samples are positioned at a slightly higher wavenumber than that of the relaxed bulk VO_2 crystal ($\sim$ 192 cm^{-1}); the B13 sample showing the biggest upshift. The $A_g(2)$ Raman mode of B0 and B13 is positioned at roughly the same wavenumber as in the relaxed VO_2 crystal (224 cm^{-1}), whereas it is positioned at a slightly lower wavenumber for B05. The $A_g(3)$ mode position ($\sim$ 309 cm^{-1} at 25 °C) is less affected, when comparing the films and the single crystal. These wavenumber positions are due to epitaxial strains created in the films. The Raman modes respect symmetry constraints and can therefore be considered as a fingerprint of the stress field stored in the films due to in- and out-of-plane strains

imposed by the substrate.

3.3. Growth and in-plane orientations

The growth orientation of the VO_2 films and their epitaxial relationships with respect to the Al_2O_3(0001) substrate were determined by temperature-dependent X-ray diffraction at room temperature and by cycling the samples up to 90°C.

3.3.1. Growth orientations

The specular $\theta/2\theta$ scans recorded at room temperature (Fig. 5) show clear diffraction peaks from the VO_2 films and the (0001)-oriented Al_2O_3 substrate. The diffraction peaks of the VO_2 films are located at $2\theta \sim 40°$ and 86°. These positions are associated to the (020) and (040) reflections of the monoclinic M1 phase, corresponding to [010]-oriented VO_2 films. This conclusion is supported by the measurement of the (220) and its equivalent reflections, featuring an azimuthal six-fold symmetry (not shown) as a consequence of three in-plane epitaxial variants from the three equivalent orientations of VO_2 (010) planes with respect to the (0001) Al_2O_3 basal plane [38] (see also section 3.3.2 below). This growth orientation is often observed for epitaxial VO_2 films synthesized on Al_2O_3(0001) [39, 40, 41, 42, 43], meaning that the V-V *zig-zag* chains lie in the surface plane. No additional diffraction peaks are observed indicating that no other vanadium oxide phases are present at room temperature.

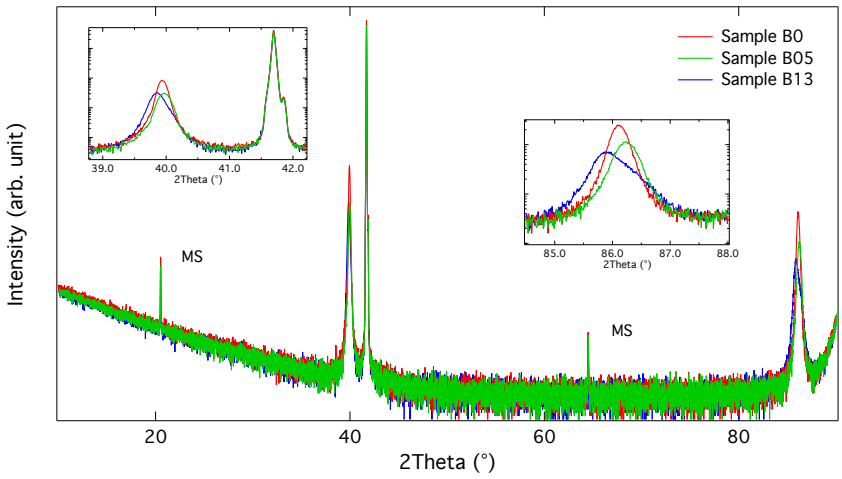

Figure 5: Specular $\theta/2\theta$ scans of the three samples at room temperature. Multiple scattering peaks from the substrate are indicated (MS). Insets are zooms on the films reflections.

The insets of Fig. 5 highlight the difference between sample diffraction peaks: while B0 and B05 exhibit a similar, single peak shape, B13 reflections have at least two components. At $\sim 86°$, B0 and B05 behave similarly with temperature, whereas B13 keeps its multi-component peak shape, even in the high temperature metallic phase (Fig. 6).

The behavior of these reflections with temperature is nonetheless qualitatively the same: the Bragg angle shifts towards lower values while heating the samples; an effect mainly dominated by the occurrence of the insulator-metal transition.

Let's first discuss the results obtained for the B0 and B05 samples. We know from Raman spectroscopy that both samples exhibit a typical M1 $\longrightarrow$ R transition with heating. Fitting the $(040)_{M1}$ reflection (Fig. 5) gives the b unit-cell parameter along the growth direction: 4.513 Å for B0 and 4.508 Å for B05. These values compare to the theoretical one for bulk VO_2 (4.538 Å), indicating a slight compressive strain along the growth direction of -0.55% for B0 and -0.66% for B05. These values are consistent with the ones already reported for films of a similar thickness [44, 45]. Given the transformation relationships between the M1 and the R phases [46], the high-temperature reflection therefore corresponds to the $(400)_R$ of the rutile tetragonal phase.

Figure 7 shows the evolution of the d_{hkl} spacing with increasing temperature of the $(040)_M$ reflection for the three samples. The occurrence of the IMT is clearly visible on the d_{hkl} values through an increase over the temperature range investigated. Finally, the $(400)_R$ Bragg peak positions were found to be equal to 86° for B0, 86.03° for B05 (1.1294 Å and 1.1291 Å in terms of d spacing). It corresponds to a_R lattice parameters of 4.518 and 4.516 Å, respectively, confirming the contraction in the out-of-plane direction ($\sim$ -0.8% compared to the bulk R phase [47]). Regarding the B13 sample, the $(040)_M$ reflection was fitted with two components, peaking at 85.88° and 86.50° (at RT). Figure 7 therefore shows the evolution with temperature of the two corresponding d_{hkl} spacings. The occurrence of the IMT is clearly visible through a more drastic increase of the d_{hkl} in the temperature region of interest.

The existence of a multiple-component peak in the case of the B13 sample would call for more investigations to be understood. However, we can draw some conclusions and propose hypotheses. First, we dismiss the possibility of an inhomogeneous introduction of boron in the VO_2 lattice leading to a strain gradient in the film thickness. Such inhomogeneous insertion was the case reported by Jia *et al.* [48] showing similar diffraction spectra for 100 keV Ne^+-implanted VO_2 films grown by PLD on Al_2O_3(0001). The implantation of Ne^+ ions led to an important lattice expansion in the direction perpendicular to the substrate and even gave rise, for the highest Ne^+ fluence, to a splitted diffraction peak with a component clearly shifted to lower Bragg angles. This Ne^+ concentration gradient in the film thickness induced a two-step insulator-metal transition, which is not observed in the B13 sample. However, the experiment of Jia *et al.* is quite different from ours where boron is incorporated at much smaller energy, simultaneously with the VO_2 growth.

Instead, we raise the hypothesis that the high-angle reflection follows the behavior of lattice parameter with the boron doping: at room temperature we measured 86.1° for B0, 86.2° for B05 and then 86.5° for B13. This reflection would be a M1 phase with a b lattice parameter that decreases with increasing boron concentration. This M1 phase

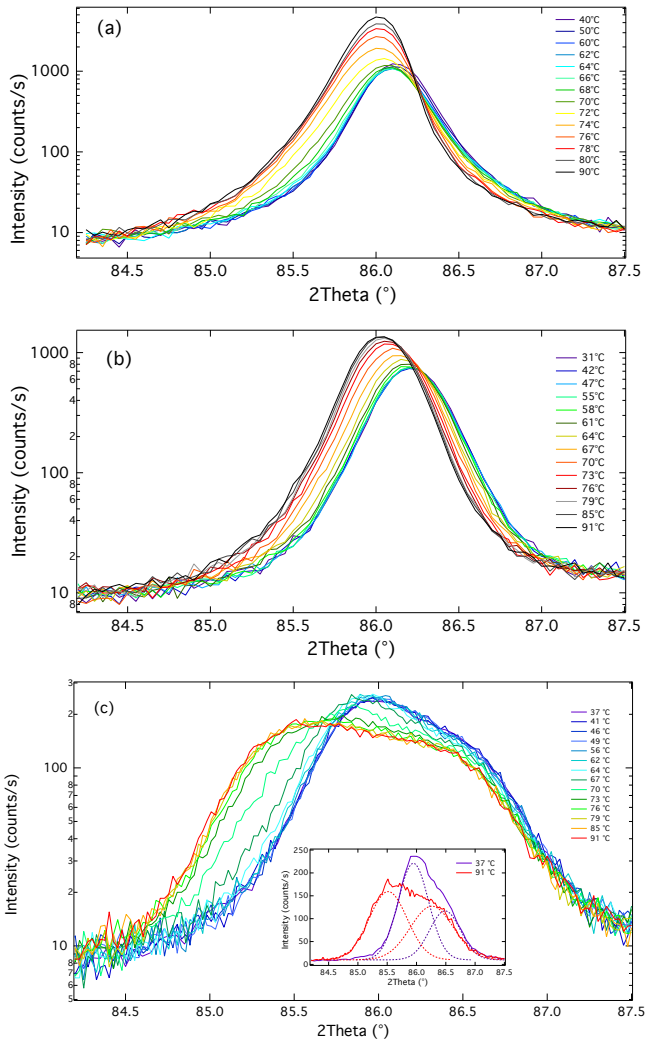

Figure 6: $(040)_M$ reflection recorded as a function of temperature during a heating step: (a) pure VO_2 (B0), (b) 0.5 at. % B-doped sample (B05), (c) 1.3 at. % B-doped sample (B13). The inset for B13 highlights the two components used for fitting the data.

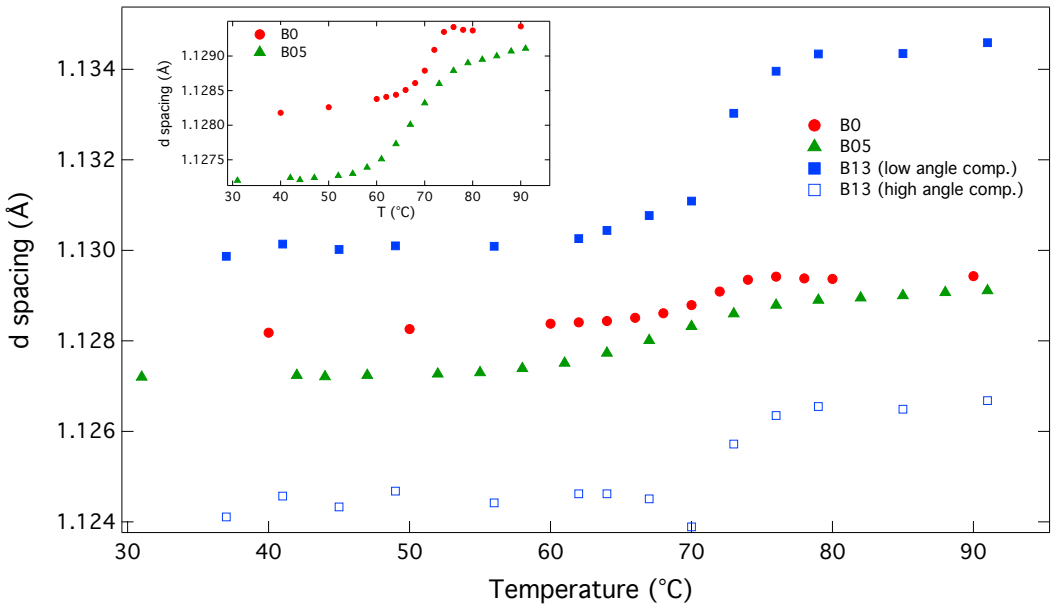

Figure 7: d spacings calculated from the 2θ positions of the $(040)_M$ reflections (heating step). The temperature-dependent curves of the B13 sample were fitted with two components, therefore leading to two distinct d spacing values.

would transform into the R phase upon heating.

	$(400)_R$	$(040)_{M1}$	$(004)_{M1}$	$(800)_{M2}$	$(004)_{M2}$
2θ (°)	85.15	85.53	85.66	85.47	85.69
d_{hkl} (Å)	1.1385	1.1344	1.1330	1.1351	1.1328

Table 1: Potential reflections between 85.5° and 86.5° and corresponding bulk values for $2\theta_B$ and d_{hkl}.

Turning to the lower angle reflection, which is more intense, it also has a very interesting behavior with temperature: it exhibits a very strong displacement at the transition, with an angular shift between room and high temperature about twice as large compared to B0 and B05 ($\sim 0.36°$ compared to 0.12° and 0.18° for B0 and B05). In fact, this displacement is of the same order than for undoped bulk VO_2. This looks like the behavior of a phase nearly free to expand out of plane, yet somehow oriented by the substrate. We believe that the situation we observe is more likely the consequence of combined strain and composition effects. In the 85.5° - 86.5° angular range, several *hkl* reflections might appear (see Tab. 1), but we definitely know from our Raman measurements that the M2 phase is present in the case of the B13 sample. We might thus assume that this low-angle contribution corresponds to the signature of the M2 phase somehow stabilized by strain effects. Despite the uncertainty remaining on the lower angle reflection

assignment, two conclusions can be drawn: i) the corresponding interplanar spacings, d_{hkl}, are systematically smaller than the theoretical ones, indicating a compressive strain along the out-of-plane direction, and ii) the axis corresponding to the V-V dimer chains always lie in the film surface plane.

3.3.2. In-plane epitaxial relationships

In a previous work, we reported on two possible in-plane epitaxial relationships for a $[010]_{M1}$-oriented VO_2 film on $Al_2O_3(0001)$ [15]. These two structural models were designated as *diagonal* and *on-axis*. The main difference in these two is the in-plane orientation of the VO_2 film, aligning either on the $[21\bar{3}0]_{Al_2O_3}$ (diagonal) or on the $[10\bar{1}0]_{Al_2O_3}$ (on-axis) crystallographic directions of the $Al_2O_3(0001)$ substrate. This leads to the following epitaxial relationships (in the rutile cell coordinates):

- for the *diagonal* model: $[011]_R \parallel [21\bar{3}0]_{Al_2O_3}$,
- for the *on-axis* model: $[010]_R \parallel [10\bar{1}0]_{Al_2O_3}$ and $[001]_R \parallel [12\bar{3}0]_{Al_2O_3}$.

These models can be disentangled by recording the $(200)_{M1}$ and $(002)_{M1}$ in-plane reflections close to the $Al_2O_3(11\bar{2}0)$ reflection. In the case of the diagonal model, a triplet and a doublet are respectively expected for these peculiar reflections, whereas it will give rise to a doublet and a singlet in the case of the on-axis model. We recorded a reciprocal space map (RSM) at room temperature for the pure VO_2 (B0) and 1.3 at. % B-doped VO_2 (B13) samples (Fig. 8). The presence of a triplet and a doublet points to the diagonal model in the case of the B0 sample, as already observed for a thicker pure VO_2 film on $Al_2O_3(0001)$ [15]. On the contrary, the B13 sample has an on-axis arrangement, as indicated by the doublet and singlet of its RSM. Figure 8 also shows the $(200)_{M1}$ and $(002)_{M1}$ reflections recorded at room temperature for the three samples. The 0.5 at. % B-doped sample shows the same signature as pure VO_2 (triplet and doublet), therefore pointing to a *diagonal* arrangement. The peaks width (roughly inversely proportional to the grains lateral size) gradually increases with the boron concentration: 2.5°, 3.2° and 4° for B0, B05 and B13, respectively. It confirms that the grain size decreases when the boron amount increases, in good agreement with the SEM images.

3.4. Conclusions

Boron-doped VO_2 films were successfully grown on $Al_2O_3(0001)$ by Pulsed Laser Deposition. We highlighted that boron insertion globally induces a decrease of the transition temperature, but a trade-off has to be found between the reduction of T_{IMT} and optimum functional properties. Indeed, although 0.5 at. % of boron improves the overall properties, further increasing the boron amount to 1.3 at. % leads to a hysteresis broadening. At this concentration, Raman spectroscopy evidences the presence of the M2 phase in addition to the M1 phase before the transition temperature, while X-ray diffraction reveals that this sample has a different in-plane epitaxial orientation with

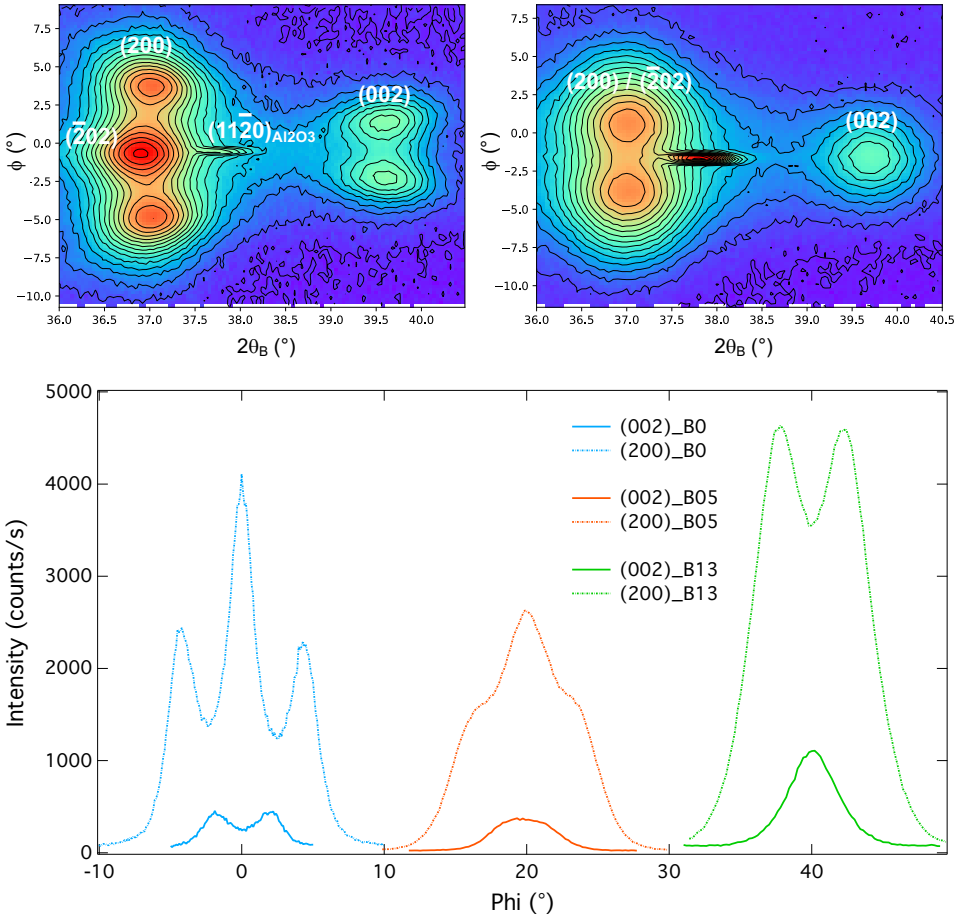

Figure 8: (top) In-plane RSMs of the B0 (left) and B13 (right) samples recorded below 50°C (in the insulating phase), close to the $(11\bar{2}0)_{Al2O3}$ substrate reflection . The *hkl* reflections of VO_2 are indexed in the monoclinic system. (bottom) Cross-sectional scans of the monoclinic reflections at room temperature. The data, centered on $\phi = 0°$, have been shifted for clarity by 20° and 40° for B05 and B13, respectively.

respect to the sapphire substrate. In the out-of-plane direction, this sample also exhibits a peculiar signature underlying the co-existence of the two phases (with one being nearly free to expand out of plane, yet somehow oriented by the substrate). The qualitatively different behaviors observed for the three films suggest that boron doping might help in tuning the functional properties according to the final application.

Acknowledgments

The LANEF framework (ANR-10-LABX-51-01) is acknowledged for its support with mutualised infrastructure, as well as the Agence Nationale de la Recherche through the ANR-15-CE08-0035 *Smart_VOx* project. We also thank Frédéric Gay (I. Néel) for his assistance in performing the *in situ* electrical measurements using the Linkam sample stage. Dr Julie Cornette and Pr Corinne Champeaux (CNRS, IRCER, Limoges) are gratefully acknowledged for their help with the FT-IR experiments.

References

[1] J. Zhou, Y. Gao, Z. Zhang, H. Luo, C. Cao, Z. Chen, L. Dai, X. Liu, Vo2 thermochromic smart window for energy savings and generation, Scientific Reports 3 (2017) 3029. URL: https://www.nature.com/articles/srep03029.

[2] M. T. Nouman, J. H. Hwang, M. Faiyaz, K.-J. Lee, D.-Y. Noh, J.-H. Jang, Vanadium dioxide based frequency tunable metasurface filters for realizing reconfigurable terahertz optical phase and polarization control, Opt. Express 26 (2018) 12922–12929. doi:doi: https://doi.org/10.1364/OE.26.012922.

[3] A. Hendaoui, N. Émond, S. Dorval, M. Chaker, E. Haddad, Enhancement of the positive emittance-switching performance of thermochromic vo2 films deposited on al substrate for an efficient passive thermal control of spacecrafts, Current Applied Physics 13 (2013) 875 – 879. URL: http://www.sciencedirect.com/science/article/pii/S1567173913000242. doi:doi: https://doi.org/10.1016/j.cap.2012.12.028.

[4] Y. Muraoka, Z. Hiroi, Metal-insulator transition of vo2 thin films grown on tio2 (001) and (110) substrates, Applied Physics Letters 80 (2002) 583–585. URL: https://doi.org/10.1063/1.1446215. doi:doi: 10.1063/1.1446215.

[5] Y. Cui, Y. Ke, C. Liu, Z. Chen, N. Wang, L. Zhang, Y. Zhou, S. Wang, Y. Gao, Y. Long, Thermochromic vo_2 for energy-efficient smart windows, Joule 2 (2018) 1707–1746. URL: https://doi.org/10.1016/j.joule.2018.06.018. doi:doi: 10.1016/j.joule.2018.06.018.

[6] C. Wu, F. Feng, J. Feng, J. Dai, L. Peng, J. Zhao, J. Yang, C. Si, Z. Wu, Y. Xie, Hydrogen-incorporation stabilization of metallic vo2(r) phase to room temperature, displaying promising low-temperature thermoelectric effect, Journal of the American Chemical Society 133 (2011) 13798–13801. URL: https://doi.org/10.1021/ja203186f. doi:doi: 10.1021/ja203186f.

[7] Y. Zhao, G. Karaoglan-Bebek, X. Pan, M. Holtz, A. A. Bernussi, Z. Fan, Hydrogen-doping stabilized metallic vo2 (r) thin films and their application to suppress fabry-perot resonances in the terahertz regime, Applied Physics Letters 104 (2014) 241901. URL: https://doi.org/10.1063/1.4884077. doi:doi: 10.1063/1.4884077.

[8] S. Chen, Z. Wang, L. Fan, Y. Chen, H. Ren, H. Ji, D. Natelson, Y. Huang, J. Jiang, C. Zou, Sequential insulator-metal-insulator phase transitions of Vo_2 triggered by hydrogen doping, Phys. Rev. B 96 (2017) 125130. URL: https://link.aps.org/doi/10.1103/PhysRevB.96.125130. doi:doi: 10.1103/PhysRevB.96.125130.

[9] J. Wan, Q. Ren, N. Wu, Y. Gao, Density functional theory study of m-doped (m = b, c, n, mg, al) vo2 nanoparticles for thermochromic energy-saving foils, Journal of Alloys and Compounds 662 (2016) 621 – 627. URL: http://www.sciencedirect.com/science/article/pii/S0925838815318909. doi:doi: https://doi.org/10.1016/j.jallcom.2015.12.100.

[10] J. J. Zhang, H. Y. He, Y. Xie, B. C. Pan, Boron-tuning transition temperature of vanadium dioxide from rutile to monoclinic phase, The Journal of Chemical Physics 141 (2014) 194707. URL: https://doi.org/10.1063/1.4901514. doi:doi: 10.1063/1.4901514.

[11] T. E. G. Alivio, D. G. Sellers, H. Asayesh-Ardakani, E. J. Braham, G. A. Horrocks, K. E. Pelcher, R. Villareal, L. Zuin, P. J. Shamberger, R. Arróyave, R. Shahbazian-Yassar, S. Banerjee, Postsynthetic route for modifying the metal—insulator transition of vo2 by interstitial dopant incorporation, Chemistry of Materials 29 (2017) 5401–5412. URL: https://doi.org/10.1021/acs.chemmater.7b02029. doi:doi: 10.1021/acs.chemmater.7b02029.

[12] K.-D. Ufert, Doping of vo2 thin films by ion implantation, physica status solidi (a) 42 (1977) 187–190. URL: https://onlinelibrary.wiley.com/doi/abs/10.1002/pssa.2210420119. doi:doi: 10.1002/pssa.2210420119.

[13] Z. Zhou, J. Li, Z. Xiong, L. Cao, Y. Fu, Z. Gao, Reducing transition temperature and diluting brown-yellow color of vo2 films via embedding ag particles periodic arrays, Solar Energy Materials and Solar Cells (2019) 110303. URL: http://www.sciencedirect.com/science/

article/pii/S0927024819306312. doi:doi: https://doi.org/10.1016/j.solmat.2019.110303.

[14] T. Hajlaoui, N. Émond, C. Quirouette, B. Le Drogoff, J. Margot, M. Chaker, Metal-insulator transition temperature of boron-doped vo2 thin films grown by reactive pulsed laser deposition, Scripta Materialia 177 (2020) 32–37. URL: http://www.sciencedirect.com/science/article/pii/S1359646219305536. doi:doi: https://doi.org/10.1016/j.scriptamat.2019.09.019.

[15] A. Bailly, S. Grenier, M. M. Villamayor, M. Gaudin, A. Y. Ramos, P. Bouvier, C. Bouchard, L. Magaud, L. Laversenne, B. Mongellaz, E. Bellet-Amalric, A. Lacoste, A. Bès, Three-phase metal-insulator transition and structural alternative for a vo2 film epitaxially grown on al2o3(0001), Journal of Applied Physics 126 (2019) 165306. URL: https://doi.org/10.1063/1.5113771. doi:doi: 10.1063/1.5113771.

[16] P. Vilanova-Martínez, J. Hernández-Velasco, A. R. Landa-Cánovas, F. Agulló-Rueda, Laser heating induced phase changes of vo2 crystals in air monitored by raman spectroscopy, Journal of Alloys and Compounds 661 (2016) 122–125. URL: http://www.sciencedirect.com/science/article/pii/S0925838815317308. doi:doi: https://doi.org/10.1016/j.jallcom.2015.11.174.

[17] M. Wojdyr, Fityk: a general-purpose peak fitting program, Journal of Applied Crystallography 43 (2010) 1126–1128. URL: https://doi.org/10.1107/S0021889810030499. doi:doi: 10.1107/S0021889810030499.

[18] A. Bradicich, H. Clarke, E. J. Braham, A. Yano, D. Sellers, S. Banerjee, P. J. Shamberger, Probing relaxation dynamics and stepped domain switching in boron-alloyed vo2, Advanced Electronic Materials 8 (2022) 2100932. URL: https://onlinelibrary.wiley.com/doi/abs/10.1002/aelm.202100932. doi:doi: https://doi.org/10.1002/aelm.202100932.

[19] P. Schilbe, Raman scattering in vo2, Physica B: Condensed Matter 316-317 (2002) 600 – 602. URL: http://www.sciencedirect.com/science/article/pii/S0921452602005847. doi:doi: https://doi.org/10.1016/S0921-4526(02)00584-7, proceedings of the 10th International Conference on Phonon Scattering in Condensed Matter.

[20] P. Schilbe, D. Maurer, Lattice dynamics in vo2 near the metal-insulator transition, Materials Science and Engineering: A 370 (2004) 449 – 452. URL: http://www.sciencedirect.com/science/article/pii/

S0921509303009407. doi:doi: https://doi.org/10.1016/j.msea.2003.08.114, 13th International Conference on Internal Friction and Ultrasonic Attenuation in Solids.

[21] J. Y. Chou, J. L. Lensch-Falk, E. R. Hemesath, L. J. Lauhon, Vanadium oxide nanowire phase and orientation analyzed by raman spectroscopy, Journal of Applied Physics 105 (2009) 034310. URL: https://doi.org/10.1063/1.3075763. doi:doi: 10.1063/1.3075763.

[22] M. Zaghrioui, J. Sakai, N. H. Azhan, K. Su, K. Okimura, Polarized raman scattering of large crystalline domains in vo2 films on sapphire, Vibrational Spectroscopy 80 (2015) 79 – 85. URL: http://www.sciencedirect.com/science/article/pii/S0924203115300096. doi:doi: https://doi.org/10.1016/j.vibspec.2015.08.003.

[23] K. Shibuya, A. Sawa, Polarized raman scattering of epitaxial vanadium dioxide films with low-temperature monoclinic phase, Journal of Applied Physics 122 (2017) 015307. URL: https://doi.org/10.1063/1.4990988. doi:doi: 10.1063/1.4990988.

[24] R. Srivastava, L. L. Chase, Raman spectrum of semiconducting and metallic vo_2, Phys. Rev. Lett. 27 (1971) 727–730. URL: https://link.aps.org/doi/10.1103/PhysRevLett.27.727. doi:doi: 10.1103/PhysRevLett.27.727.

[25] F. Gervais, W. Kress, Lattice dynamics of oxides with rutile structure and instabilities at the metal-semiconductor phase transitions of nbo_2 and vo_2, Phys. Rev. B 31 (1985) 4809–4814. URL: https://link.aps.org/doi/10.1103/PhysRevB.31.4809. doi:doi: 10.1103/PhysRevB.31.4809.

[26] C. Marini, E. Arcangeletti, D. Di Castro, L. Baldassare, A. Perucchi, S. Lupi, L. Malavasi, L. Boeri, E. Pomjakushina, K. Conder, P. Postorino, Optical properties of $v_{1-x}cr_xo_2$ compounds under high pressure, Phys. Rev. B 77 (2008) 235111. URL: https://link.aps.org/doi/10.1103/PhysRevB.77.235111. doi:doi: 10.1103/PhysRevB.77.235111.

[27] A. C. Jones, S. Berweger, J. Wei, D. Cobden, M. B. Raschke, Nano-optical investigations of the metalinsulator phase behavior of individual vo2 microcrystals, Nano Letters 10 (2010) 1574–1581. URL: https://doi.org/10.1021/nl903765h. doi:doi: 10.1021/nl903765h.

[28] E. Strelcov, A. Tselev, I. Ivanov, J. D. Budai, J. Zhang, J. Z. Tischler, I. Kravchenko, S. V. Kalinin, A. Kolmakov, Doping-based stabilization of the m2 phase in free-standing vo2 nanostructures at room temperature, Nano Letters 12 (2012) 6198–6205. URL: https://doi.org/10.1021/nl303065h. doi:doi: 10.1021/nl303065h.

[29] I. N. Goncharuk, A. V. Ilinskiy, O. E. Kvashenkina, E. B. Shadrin, Electron-electron correlations in raman spectra of vo2, Physics of the Solid State 55 (2013) 164–174. URL: https://doi.org/10.1134/S1063783413010149. doi:doi: 10.1134/S1063783413010149.

[30] J. C. Parker, Raman scattering from vo_2 single crystals: A study of the effects of surface oxidation, Phys. Rev. B 42 (1990) 3164–3166. URL: https://link.aps.org/doi/10.1103/PhysRevB.42.3164. doi:doi: 10.1103/PhysRevB.42.3164.

[31] S. Zhang, J. Y. Chou, L. J. Lauhon, Direct correlation of structural domain formation with the metal insulator transition in a vo2 nanobeam, Nano Letters 9 (2009) 4527–4532. URL: https://doi.org/10.1021/nl9028973. doi:doi: 10.1021/nl9028973.

[32] M. Balkanski, R. F. Wallis, E. Haro, Anharmonic effects in light scattering due to optical phonons in silicon, Phys. Rev. B 28 (1983) 1928–1934. URL: https://link.aps.org/doi/10.1103/PhysRevB.28.1928. doi:doi: 10.1103/PhysRevB.28.1928.

[33] K. Okimura, N. Hanis Azhan, T. Hajiri, S.-i. Kimura, M. Zaghrioui, J. Sakai, Temperature-dependent raman and ultraviolet photoelectron spectroscopy studies on phase transition behavior of vo2 films with m1 and m2 phases, Journal of Applied Physics 115 (2014) 153501. URL: https://doi.org/10.1063/1.4870868. doi:doi: 10.1063/1.4870868.

[34] S.-J. Chang, W.-K. Hong, H. J. Kim, J. B. Lee, J. Yoon, H. C. Ko, Y. S. Huh, Probing the photothermally induced phase transitions in single-crystalline vanadium dioxide nanobeams, Nanotechnology 24 (2013) 345701. doi:doi: 10.1088/0957-4484/24/34/345701.

[35] J. M. Atkin, S. Berweger, E. K. Chavez, M. B. Raschke, J. Cao, W. Fan, J. Wu, Strain and temperature dependence of the insulating phases of vo2 near the metal-insulator transition, Phys. Rev. B 85 (2012) 020101. URL: https://link.aps.org/doi/10.1103/PhysRevB.85.020101. doi:doi: 10.1103/PhysRevB.85.020101.

[36] M. Nazari, Y. Zhao, V. Hallum, A. A. Bernussi, Z. Y. Fan, M. Holtz, Finite size effect on the phase transition of vanadium dioxide, Applied Physics Letters 103 (2013) 043108. URL: https://doi.org/10.1063/1.4816507. doi:doi: 10.1063/1.4816507.

[37] A. Tselev, I. A. Luk'yanchuk, I. N. Ivanov, J. D. Budai, J. Z. Tischler, E. Strelcov, A. Kolmakov, S. V. Kalinin, Symmetry relationship and strain-induced transitions

between insulating m1 and m2 and metallic r phases of vanadium dioxide, Nano Letters 10 (2010) 4409–4416. URL: https://doi.org/10.1021/nl1020443. doi:doi: 10.1021/nl1020443.

[38] C. Chen, Y. Zhu, Y. Zhao, J. H. Lee, H. Wang, A. Bernussi, M. Holtz, Z. Fan, Vo2 multidomain heteroepitaxial growth and terahertz transmission modulation, Applied Physics Letters 97 (2010) 211905. URL: https://doi.org/10.1063/1.3519361. doi:doi: 10.1063/1.3519361.

[39] V. Théry, A. Boulle, A. Crunteanu, J. C. Orlianges, A. Beaumont, R. Mayet, A. Mennai, F. Cosset, A. Bessaudou, M. Fabert, Role of thermal strain in the metal-insulator and structural phase transition of epitaxial vo2 films, Phys. Rev. B 93 (2016) 184106. URL: https://link.aps.org/doi/10.1103/PhysRevB.93.184106. doi:doi: 10.1103/PhysRevB.93.184106.

[40] K. Okimura, J. Sakai, Changes in lattice parameters of vo2 films grown on c-plane al2o3 substrates across metal–insulator transition, Japanese Journal of Applied Physics 48 (2009) 045504. URL: http://stacks.iop.org/1347-4065/48/i=4R/a=045504.

[41] K. Okimura, J. Sakai, S. Ramanathan, In situ x-ray diffraction studies on epitaxial vo2 films grown on c-al2o3 during thermally induced insulator-metal transition, Journal of Applied Physics 107 (2010) 063503. URL: https://doi.org/10.1063/1.3327422. doi:doi: 10.1063/1.3327422.

[42] F. J. Wong, Y. Zhou, S. Ramanathan, Epitaxial variants of vo2 thin films on complex oxide single crystal substrates with 3m surface symmetry, Journal of Crystal Growth 364 (2013) 74–80. URL: http://www.sciencedirect.com/science/article/pii/S0022024812008639. doi:doi: https://doi.org/10.1016/j.jcrysgro.2012.11.054.

[43] Z. P. Wu, S. Yamamoto, A. Miyashita, Z. J. Zhang, K. Narumi, H. Naramoto, Single-crystalline epitaxy and twinned structure of vanadium dioxide thin film on (0001) sapphire, Journal of Physics: Condensed Matter 10 (1998) L765. URL: http://stacks.iop.org/0953-8984/10/i=48/a=002.

[44] J. Jian, X. Wang, L. Li, M. Fan, W. Zhang, J. Huang, Z. Qi, H. Wang, Continuous tuning of phase transition temperature in vo2 thin films on c-cut sapphire substrates via strain variation, ACS Applied Materials and Interfaces 9 (2017) 5319–5327. URL: https://doi.org/10.1021/acsami.6b13217. doi:doi: 10.1021/acsami.6b13217.

[45] V. Théry, A. Boulle, A. Crunteanu, J. C. Orlianges, A. Beaumont, R. Mayet, A. Mennai, F. Cosset, A. Bessaudou, M. Fabert, Structural and electrical properties of large area epitaxial vo2 films grown by electron beam evaporation, Journal of Applied Physics 121 (2017) 055303. URL: https://aip.scitation.org/doi/10.1063/1.4975117.

[46] M. Marezio, D. B. McWhan, J. P. Remeika, P. D. Dernier, Structural aspects of the metal-insulator transitions in cr-doped vo2, Phys. Rev. B 5 (1972) 2541–2551. URL: https://link.aps.org/doi/10.1103/PhysRevB.5.2541. doi:doi: 10.1103/PhysRevB.5.2541.

[47] K. Rogers, An x-ray diffraction study of semiconductor and metallic vanadium dioxide, Powder Diffraction 8 (1993) 240. URL: https://doi.org/10.1017/S0885715600019448. doi:doi: https://doi.org/10.1017/S0885715600019448.

[48] Q. Jia, J. Grenzer, H. He, W. Anwand, Y. Ji, Y. Yuan, K. Huang, T. You, W. Yu, W. Ren, X. Chen, M. Liu, S. Facsko, X. Wang, X. Ou, 3d local manipulation of the metal–insulator transition behavior in vo2 thin film by defect-induced lattice engineering, Advanced Materials Interfaces 5 (2018) 1701268. URL: https://doi.org/10.1002/admi.201701268. doi:doi: 10.1002/admi.201701268.